Ceramics International 47 (2021) 23803–23813

Contents lists available at ScienceDirect

Ceramics International

journal homepage: www.elsevier.com/locate/ceramint

YAG thermal barrier coatings deposited by suspension and solution precursor thermal spray

T.A. Owoseni [a], A. Rincon Romero [a], Z. Pala [b], F. Venturi [a], E.H. Lester [a], D.M. Grant [a], T. Hussain [a,*]

[a] Faculty of Engineering, University of Nottingham, Nottingham, NG7 2RD, UK
[b] GE Aviation, Beranovych 65, Prague, Czech Republic

ARTICLE INFO

Keywords:
YAG phase Transition
New generation-TBC
SHVOF
Single splat

ABSTRACT

Yttrium aluminium garnet (YAG) is a promising topcoat material for thermal barrier coatings due to its high temperature stability and better CMAS (calcium-magnesium-alumino-silicate) resistance. YAG topcoats were deposited by suspension and solution precursor high-velocity oxy-fuel (HVOF) thermal spray. The relationships between processing, microstructure and final properties were studied through a range of characterization techniques and thermal cycling tests. The microstructure of the as-sprayed YAG topcoat from stoichiometric solution precursor (SP-YAG) had distributed pores and inter-splat boundaries, while the as-sprayed topcoat produced from suspension (S-YAG) had vertical and branched micro cracks, pores, and inter-splat boundaries. Both as-sprayed coatings were composed of amorphous phase, hexagonal yttrium aluminium perovskite (YAP) and cubic YAG. In thermal cycling tests, 20% of SP-YAG failure was reached after the 10th cycle; whereas, S-YAG reached the failure criteria between the 60th and 70th cycle. The failure of both the SP-YAG and the S-YAG topcoats occurred due to thermal stresses during the thermal cycling.

1. Introduction

Thermal barrier coating (TBC) systems consist of a refractory topcoat and a metallic alloy bond coat to protect the superalloy substrates (blades and vanes) in gas turbines from high temperatures [1]. The effectiveness of the TBC systems relies on the integrity of the topcoat specified by phase stability, thermal conductivity, low weight, high strain tolerance, coefficient of thermal expansion (CTE), resistance to ambient and high temperature corrosion and chemical compatibility with the underlying bond coat and the TGO—a protective oxide [2]. The bond coat, typically MCrAlY where M stands for Ni/Co, functions as the oxidation-resistant layer of the TBC system and it forms a thermally grown oxide (TGO, typically alumina) as a layer between the bond coat surface and the topcoat [1].

Yttria stabilized zirconia (YSZ) has been the standard material for TBC due to its low thermal conductivity, high melting point, high coefficient of thermal expansion and low density [1,3]. The microstructure of atmospheric plasma spray (APS) deposited YSZ has distributed intersplat boundaries, pores [4] and segmented vertical cracks [5]. In contrast, electron beam physical vapour deposition (EB-PVD) deposited YSZ presents a feathery microstructure of columnar YSZ grains (2–10 μm in diameter) with globular and spheroid pores [6]—both APS and EB-PVD are the standard topcoat deposition processes. The microstructures of either APS YSZ or EB-PVD YSZ topcoats allows oxygen transport through the topcoat by gas permeation [7]. The bond coat thereby releases its aluminium content to form a layer of alumina as the TGO—the formation and growth rate of the TGO limits the durability of the TBC system [8].

Besides the issue of oxygen conduction through the microstructure, YSZ also experiences undesirable phase transitions. The metastable tetragonal (t') phase at temperatures around 1200 °C transforms into cubic (c) and tetragonal (t) phases. The tetragonal t phase can evolve further to monoclinic (*m*) phase that comes with 3–5% volumetric changes, which induces cracks within the YSZ coating leading to its spallation [9]. This phase transformation could also be induced by a calcium magnesium-alumino-silicate (CMAS) attack. Molten CMAS dissolves YSZ through selective removal of yttrium ions in the YSZ structure-this destabilizes the metastable tetragonal phase and results in its transformation to monoclinic phase [10]. CMAS is found in volcanic ash, sand and runway rubbles; it infiltrates the topcoat from the air

* Corresponding author.
E-mail address: Tanvir.Hussain@nottingham.ac.uk (T. Hussain).

https://doi.org/10.1016/j.ceramint.2021.05.087
Received 16 April 2021; Accepted 11 May 2021
Available online 13 May 2021

carried into the turbine engine [2]. Again, YSZ coatings sinter at temperatures from 1000 °C: this causes densification in nanostructured YSZ coatings [11] and necking in the atmospheric plasma (APS) sprayed YSZ coatings [12]. The necking reduces the strain tolerance of the APS YSZ coating leading to increased stiffness and internal stress—a phenomenon that compromises the thermal cyclic life of the coating. This has spurred the search for new topcoat materials and/or processing techniques to find alternative materials that could resist oxygen transport, CMAS attack, phase transition and sintering at elevated temperature—this will lead to the development of the next generation of thermal barrier coatings.

Padture and Klemens [13] proposed yttrium aluminium garnet (YAG) as an alternative TBC topcoat material because of its lower oxygen diffusivity (10^{-20} m^2/s) compared to YSZ (10^{-10} m^2/s); it also presents better phase stability at high temperature [14,15], resistance to sintering and CMAS attack. In addition, YAG is not prone to react with the thermally grown oxide (TGO) layer [16,17]. However, the microstructure of YAG coating must be carefully engineered without compromising durability—since a porous coating allows influx of oxygen and CMAS materials [7].

There are several manufacturing processes out there to deposit YAG coatings. The first TBC work to incorporate YAG was a multilayer TBC produced by a small particle plasma spray process—a variant of APS [14]. A porous YAG coating (10 μm) was sandwiched between layers of YSZ coating (30 and 200 μm) for phase stability, and in another architecture, the 10 μm porous YAG coating was deposited on an 80 μm thick YSZ coating for oxidation protection. The YAG layer, although porous, prevents Y_2O_3 depletion at the YSZ/YAG interface to ensure phase stability for the YSZ in the sandwich architecture; it also slows down the TGO growth rate in the latter architecture by a factor of about three. A columnar YAG coating with some YAP, YAM and Y_2O_3 was produced by electrostatic spray-assisted vapour deposition (ESAVD) using solution precursor—ESVAD forms coatings from vaporized precursor droplets charged in an electric field to undergo decomposition and/or chemical reactions [18]. The coating has uniformly distributed inter-columnar spacing of 2 μm which would aid oxygen influx to the bond coat. The ESAVD technique could be a means to produce strain compliant YAG coating, but it has low deposition efficiency; besides the coating needs to be heat treated at 700–900 °C to form pure YAG. Kumar et al. [17,19,20] reported YAG TBC deposited by solution precursor plasma spray (SPPS). The YAG TBC was engineered to possess a stack of horizontal micro pores which they termed inter-pass boundaries. The inter-pass boundaries were shown to support the low thermal conductivity and strain compliance of the coating that ensures its durability supersedes APS YSZ with or without CMAS presence.

Weyant and Faber [7] studied APS deposited YAG to provide a model through the design of experiment (DoE) that links microstructure features with plasma spray process parameters. The flame power and the standoff distance was found to control the porosity and the crystallinity of the YAG coating, using powder with the standard particle size range. However, the amorphous coatings would crystalize to YAG in ~ 18 min at 900 °C without sintering. Gu et al. [21] sprayed composite YAG/YSZ coating using APS with a varying mix of the YAG and YSZ powders. The composite coating is dense with amorphous YAG, crystalline YAG and YAP phases in crystalline YSZ coating. YSZ suppresses the crystallization of the amorphous YAG; even at 1200 °C it takes 12 h to achieve full crystallinity as against pure amorphous YAG coating, which crystalizes in 30 min at 920 °C. The crystallization process of the amorphous YAG in the composite coating also initiates and propagates micro cracks that would form oxygen pathway to the bond coat.

However, with the continued interest in YAG based TBC topcoats, high velocity oxy-fuel (HVOF) thermal spray could provide alternative microstructures based on an effective combination of materials and processing technique. Suspension HVOF thermal spray deposits denser coatings with finer pores using suspension feedstock compared to powder-based spray [22]. In addition, solution precursor-based spray provides process efficiency that eliminates the initial suspension production route for nano structured coatings. This work presents two TBC topcoats deposited by high-velocity oxy-fuel (HVOF) thermal spray: one from stoichiometric solution precursor of $Al(NO_3)_3 9H_2O$ and $Y(NO_3)_3.6H_2O$ that produces YAG and the other from a suspension of yttrium aluminium garnet (YAG). The microstructure of HVOF sprayed YAG coatings was investigated based on materials processing routes. The as-sprayed and thermally cycled topcoats were studied to understand the coating formation process and the failure modes under thermal cycling.

2. Methodology

2.1. Materials

An aqueous YAG suspension supplied by Baikowski (Sillingy Cedex, France) with particle size distribution of $D_{50} = 0.09$ μm was used in this study. The as-supplied suspension with a solid loading of 50 wt % was further diluted with water into a 20 wt % solid loading to ensure better flow during the spray process. No additional dispersants were used as the commercial suspension already have organic additives that help his stabilization.

The solution precursor was made by dissolving it in water, with a stoichiometry proportion to achieve YAG, aluminium nitrate nonahydrate ($Al(NO_3)_3{\cdot}9H_2O$) and yttrium nitrate hexahydrate ($Y(NO_3)_3{\cdot}6H_2O$) [23], both supplied by Fisher Scientific (Loughborough, UK).

Stainless steel and Ni-alloy were used as substrates in the deposition of the coatings. The stainless steel used was cold rolled AISI 304 (60 × 25 × 2 mm) with a nominal composition of 19.0 Cr, 9.3 Ni, 0.05 C and the balance is Fe (in wt. %) (Unicorn, UK); a Ni-alloy, Hastelloy C-263 grade, (nominal compositions in wt. % of 0.5 Al, 2.2 Ti, 20.4 Cr, 0.5 Fe, 20.2 Co, 6.0 Mo; the balance is Ni) was used as the base metal for the samples to be used in the thermal cycling experiment. Some of the stainless-steel substrates were grit blasted and cleaned in industrial methylated spirit (IMS) in an ultrasonic bath for 10 min for the primary coating deposition. The grit blasting was done at 3 bar with fine alumina particles (0.125–0.149 mm) using a grit blaster from Guyson (Dudley, England). Another set of stainless-steel substrates was polished to 1 μm finish to collect splats of the deposited YAG coatings while the grit blasted ones were used for the full coating deposition. The Ni-alloy used was pre-coated with CoNiCrAlY (Co-210-24, Praxair Surface Technologies, Germany) bond coat with nominal composition in wt. % (38.5 Co, 32.0 Ni, 21.0 Cr, 8.0 Al and 0.5 Y) using a kerosene fuelled HVOF spray technique. The deposition conditions and detail study of the bond coat can be found in the work of Saeidi et al. [24].

2.2. Solution precursor preparation and chemical analysis

1 M of $Al(NO_3)_3{\cdot}9H_2O$ and 0.6 M of $Y(NO_3)_3{\cdot}6H_2O$ water-based solutions were mixed to have a 1L solution precursor with a molarity ratio 5:3 (see Table 1). A selected solution precursor aliquot was dried in a furnace at 80 °C for 24 h. The dried samples were used for differential thermal analysis on a simultaneous TGA/DSC (SDT Q600, TA Instruments, USA) from ambient temperature to 1000 °C at a heating rate

Table 1
Parameters of the stoichiometry solution of the precursor salts.

Solution parameters	$Al(NO_3)_3 .9H_2O$	$Y(NO_3)_3 .6H_2O$
Concentration, M	1	0.6
Volume of DI water, ml	500	500
Mass of solute, g	187.56	114.90
Concentration after mixing, M	0.5	0.3
Stoichiometric mix ratio for YAG synthesis	5	3
pH	2.04	2.44

of 10 °C/min in flowing air. Selected dried samples were then calcined in a box furnace at 450, 750 and 900 °C for 3 h using a heating rate of 10 °C/min. The calcined samples were grounded into powder for FTIR and X-ray diffraction analysis.

FTIR spectra for the samples calcined at temperatures 450 °C, 750 °C and 900 °C were collected using a spectrophotometer (Tensor 27) supplied by Bruker (Coventry, UK). The spectra were collected in absorbance mode over the wavenumber range of 400–4000 cm^{-1} at a resolution of 4 cm^{-1} and acquiring 64 scans per spectrum.

2.3. Coatings deposition

All coatings were sprayed using a modified TopGun SS (GTV GmbH, Germany) with an axial injection of suspension or solution precursor directly into the combustion chamber with a 0.3 mm diameter nozzle. The suspension and/or solution precursor was delivered from a pressurized vessel maintained at 5 bar. The substrates were mounted onto a rotating carousel (~260 mm) with a vertical axis of rotation of 73 rpm and equivalent substrate speed of 1 m/s while the spray gun traversing vertically at a speed of 5 mm s^{-1}. In the case of the single splat spray test, the 1 μm-polished substrates were spun at 100 rpm with the spray gun traversing vertically at a speed of 30 mm s^{-1} to ensure only few splats were collected. The complete spray set up was further described elsewhere [11]. Table 2 shows the spray parameters for all the coatings—the YAG coating obtained from the solution precursor will be called SP-YAG while the one from YAG suspension will be referred to as S-YAG.

2.4. Diagnostic characteristics of in-flight particles

The inflight particle velocity and the temperature was obtained using Accuraspray 4.0 from Tecnar (St. Bruno, Canada). The equipment consists of an optoelectronics sensor system with an attached coupled-charged-device (CCD) camera and a two-colour pyrometer. The CCD camera enables the analysis of the flame appearance vis-a-vis position, width, distribution and intensity—referred to as the plume density. The spray conditions for the suspension and solution precursor were maintained (Table 2) for each set of data acquired. The equipment provides ensemble measurement of particles in a control volume (3.2 mm × 10 mm x 25 mm) of spray jet rather than a single particle [25]. Multiple measurements (~60) are taken at a reaction time of 5 s with a signal amplification of 24–27 times and camera exposure time of 41 ms. The velocity and temperature values recorded represents the average for the particles in the control volume. Each temperature and velocity measurement was taken will have an associated measurement error ± 3% to account for the accuracy of the instrument.

2.5. Microstructural characterization

The commercial YAG suspension was heated separately in a box furnace at 100 °C for 8 h to obtain dried powder for secondary electron (SE) images on the Scanning Electron Microscope (SEM) and X-ray diffraction analysis. Cross-sections of the coatings were prepared by standard metallographic procedures; backscattered electron (BSE magnifications 700x) images were used to measure coating thickness using the image analysis software Image-J (NIH, USA). The reported thickness is the average of at least 5 measurements. Fractured surfaces of the coatings were prepared from notched samples (5 × 25 × 2 mm) of coated stainless-steel substrates cooled in liquid nitrogen for 5–10 min and bent in a vice to fracture at the notch. The SEM images were obtained using JEOL 6490 SEM from JEOL Ltd. (Tokyo, Japan) at 20 kV and a working distance of 10 mm.

Table 2
Deposition parameters for SHVOF sprayed suspension YAG and solution precursor YAG.

Parameters	SP-YAG	S-YAG
Hydrogen flow rate, l/min.	612	612
Oxygen flow rate, l/min.	306	306
Flame power, kW	101	101
Suspension flow rate, ml/min.	50	50
Spray distance, mm	85	85
Number of passes	20	40

The powders, calcined samples and coatings were scanned on Bruker D8 Advance DaVinci X-ray diffractometer (Coventry, England) with a Cu K_α radiation source (1.54 Å) in Bragg-Brentano configuration. The instrument has a LYNXEYE XE-T high energy resolution 1D x-ray detector, which allows rapid data collection. The scans were completed within 10-80° 2θ, a step of 0.02° and dwell of 1 s/step. The phase identification of the XRD results was completed using EVA programme package supported by data from the PDF-2 database. Quantitative Rietveld refinement of the XRD data was performed with TOPAS (Coelho Software, Australia) to obtain the degree of crystallinity and phase quantification in the coatings and the calcined samples [26].

2.6. Thermal cycling test

The thermal cycling test samples were conducted on 10 mm diameter discs cut from samples deposited onto the bond coat deposited Ni-alloy substrates. The SP-YAG was cut by electro-discharge machining (EDM) while the S-YAG was cut by water-jet abrasive because it was insulating. The cyclic tests were carried out in a bottom-loading isothermal furnace (CM Furnaces Inc., Bloomfield, NJ) in 80-min cycles. Each cycle consisted of 10-mins heat-up to 1100 °C, 40-mins dwelling at the maximum temperature, and 30-min of forced air-cooling; the cooling ensured the samples reached ~ 80 °C before a reheating. 3 SP-YAG and 2 S-YAG samples were used to conduct the test. The samples were examined after 5 and 10 cycles and after the 10th cycle every 10 cycles. The failure analysis was conducted on the top surface and on the cross-section of the samples after the cycle of failure. The failure criterium was established after 20% of failure is detected on the topcoat.

3. Results

3.1. YAG synthesis from solution precursors

The combined plot of the thermogravimetric (TG) and the differential scanning calorimetry (DSC) plots of the solution precursor are shown in Fig. 1(a), where the upward direction indicates the evolution of exothermic effects. The DTG graph shows the combined weight loss of ~ 56% due to evaporation of absorbed water, molecular water, and decomposition of the nitrate from 50 °C to end at ~ 650 °C, which is consistent with the four successive endothermic peaks shown in the DSC plot in the same temperature range. A clear crystallization exothermic effect could be detected on the peak centred at around 940 °C.

The FTIR spectra of the solution precursor and the samples calcined at three different temperatures are shown in Fig. 1(b). The spectrum for the solution precursor shows a wide band between 3000 and 3700 cm^{-1}, assigned to stretching vibration of O–H groups and a band at 1640 cm^{-1} associated to the bending mode of water, while two vibration bands centred at ~ 1400 cm^{-1} and ~ 1250 cm^{-1} associated with the anti-symmetric stretching vibration mode of the nitrate group. Other weaker vibration bands assigned to the Al–O and Y-O bonding vibration appear between 900 and 550 cm^{-1}. The nitrate vibration bands weaken as temperature increased; at 900 °C the spectrum shows the characteristic vibrations of YAG, it shows the Al-O metal-oxygen vibration stretching bands at 788 cm^{-1} and 688 cm^{-1}, while the Y-O vibration appears at the 722 cm^{-1}. The band at the 567 cm^{-1} represents another Y-O [23,27].

Fig. 2 shows the XRD diffractograms of the calcined samples. No crystallization has occurred for the calcination at 450 °C and 750 °C, and both diffractograms presented two broad amorphous humps between 20°-40° and 40°-70° 2θ respectively. The calcination done at 900 °C

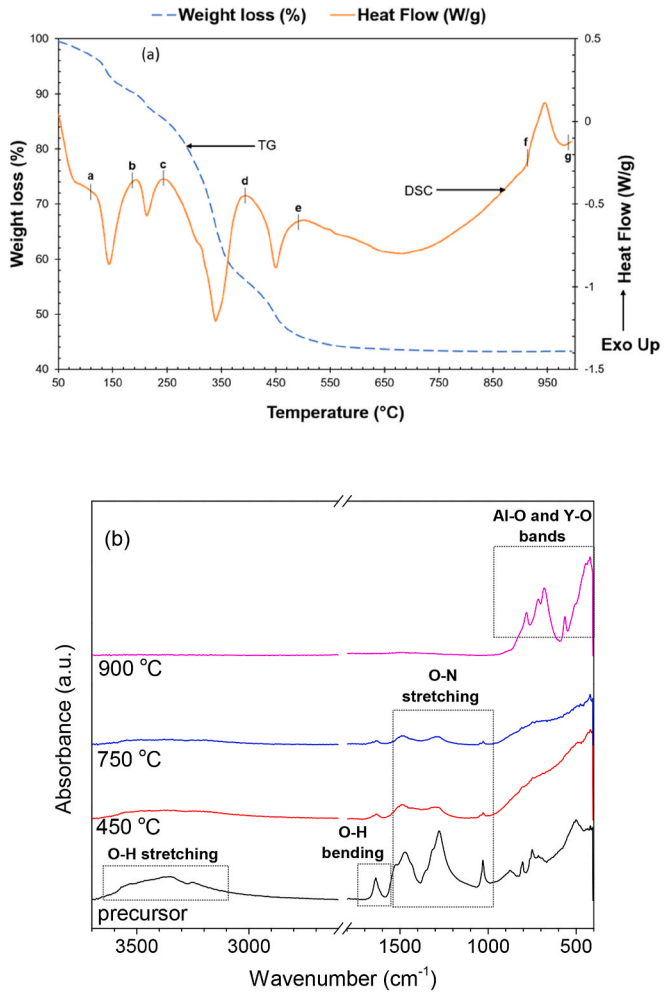

Fig. 1. (a) Combined plot of the thermogravimetric (TG) and the differential scanning calorimetry (DSC) of the solution precursor showing percent water loss (56.19%) from the sample, the endothermic peaks (a-b, b-c, c-d, d-e) and the exothermic peak (f–g) respectively. (b) FTIR spectra of the solution precursor and the sols calcined at different temperatures (450 °C, 750 °C and 900 °C).

produced cubic YAG as the only crystalline phase—the indexes were based on ICSD PDF card 01-082-0575.

3.2. Microstructure and phase composition of YAG feedstock and YAG coatings from suspension and solution precursor

3.2.1. YAG feedstock

The characterization of the YAG particles in the as-received YAG suspension is shown in Fig. 3. The particles presented spherical shapes (Fig. 3(a)), with the size of the constitutive particle being ~ 100 nm (Fig. 3(b)). The particle size distribution in the as-received suspension is shown in Fig. 3(c), depicting D_{10}, D_{50} and D_{90} to be 1.37 μm, 5.08 μm and 11.36 μm, respectively. The Rietveld refinement analysis of the powder from the as-received YAG suspension shows the presence of two crystalline phase compositions. The powder particles consist of ~98% cubic YAG; the powder contains some Y_2O_3 impurities, which makes the balance, as shown in Fig. 3(c). The crystallite size of the cubic YAG phase as analysed gives 92 ± 5 nm; this is very close to the 100 nm estimate for the individual particles in the agglomerate identified in the SEM micrograph of the particles.

3.2.2. Microstructure of as-sprayed SP-YAG and S-YAG coatings

The constitutive features of the SP-YAG and the S-YAG coatings

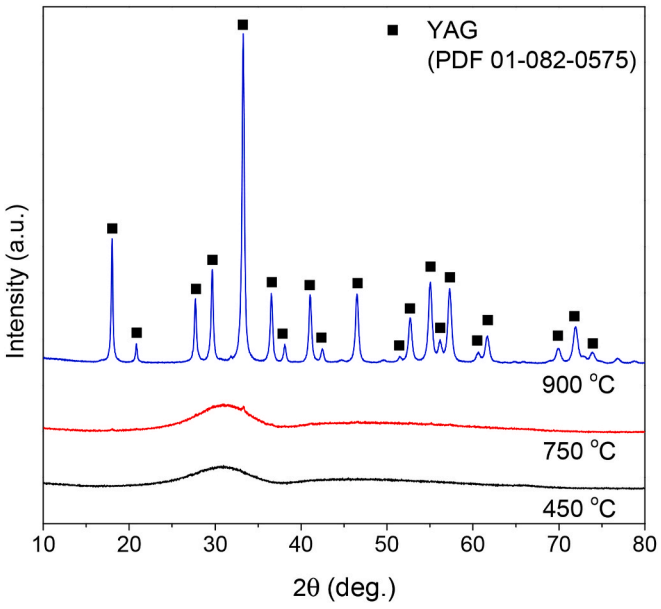

Fig. 2. XRD scan profile of sols calcined at 450, 750 and 900 °C.

(splats and lamellae) are presented in Figs. 4 and 5. The SP-YAG splats collected from the single pass of the fast-traversed gun are shown in Fig. 4(a); the splats formed from molten particles into irregular morphology and varying sizes. The pile of the splats built dense lamellae with submicron and micron size intra-lamellar voids as in the fractograph shown in Fig. 4(b). Similarly, the S-YAG splats collected from the single pass of the fast-traversed gun are shown in Fig. 5(a); molten particles impact the substrate to form splats of varying sizes and morphology. The splats built dense lamellae with micron size intra-lamellar voids as in the fractograph shown in Fig. 5(b). The lamella size of the S-YAG is ~ 25 μm as against ~ 5 μm in the SP-YAG.

The temperature and velocity of the molten particles impacting the substrate to form the splats were measured at spray distance. The values for the SP-YAG are 1623 ± 49 °C and 855 ± 26 m/s while the S-YAG molten particles have 1992 ± 60 °C and 855 ± 27 m/s respectively; the associated imprecisions are due to the accuracy of the instrument, as presented in sub-section 2.4. In addition, the measurement is taken as an average value of the particles in a determined volume, and certainly not the specific temperature of each particle.

The BSE micrographs of the cross-section of the two coatings are shown in Fig. 6. The micrograph of the SP-YAG coating in Fig. 6(a) shows the three layers of the TBC system: the SP-YAG topcoat, the MCrAlY bond coat and the Ni-super alloy substrate. The SP-YAG topcoat has a thickness of 33 ± 1 μm; the higher magnification image in Fig. 6(b) shows randomly distributed pores, inter splat boundaries and it shows no crack nor delamination at the interface with the bond coat. Fig. 6(c) shows the micrograph of the S-YAG with the S-YAG topcoat, the MCrAlY bond coat and the Ni-superalloy substrate. The topcoat microstructural features present inter-splat boundaries, pores, vertical and horizontal micro cracks. The S-YAG topcoat has a thickness of 139 ± 4 μm, showing good interface adhesion with the bond coat with no observable cracks or delamination.

The elemental composition of the SP-YAG (Fig. 6(b)) and S-YAG (Fig. 6(c)) topcoats are presented in Table 3. The carbon picked up from the carbon coating of the samples was excluded from the analysis. Both coatings contain similar proportions of the three major elements in the yttrium-aluminium system (Al, Y, and O) in a ratio quite close to the one of the YAG phase.

The top surface morphologies of the two coatings are presented in Fig. 7. The two coatings have randomly distributed bumps throughout the spread of their surfaces. The bumps on the SP-YAG coating (Fig. 7

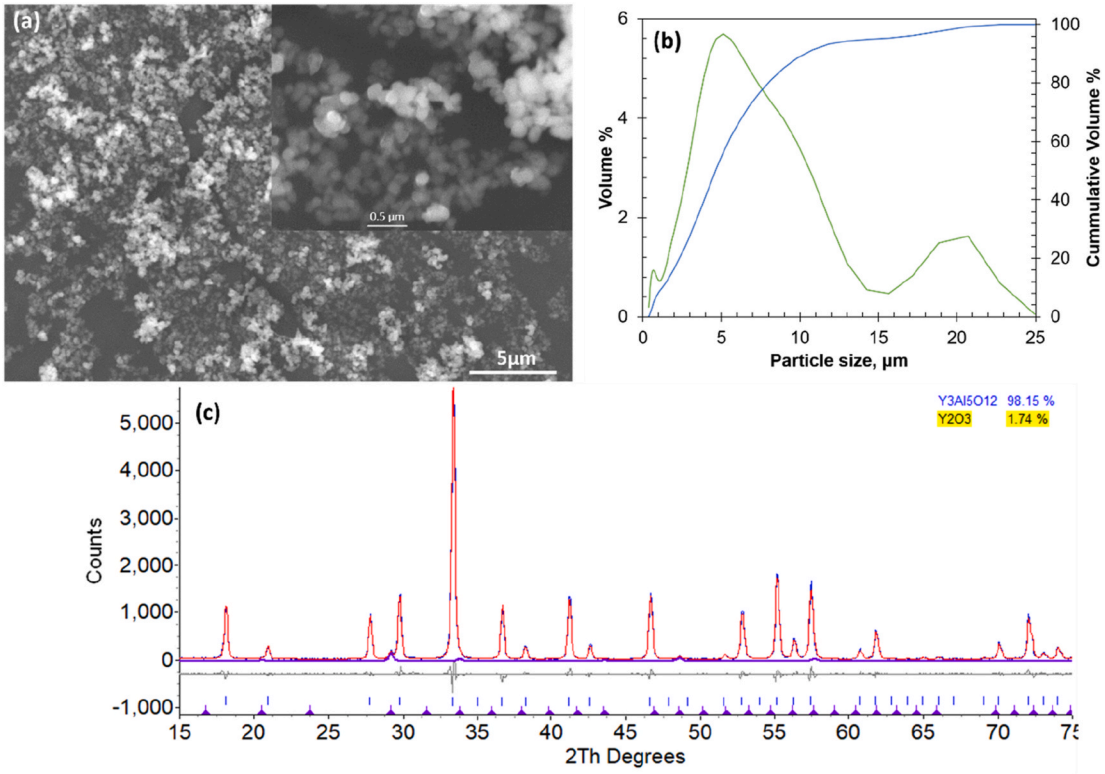

Fig. 3. (a) SE SEM micrograph showing agglomerates of YAG particles dried out from the as-received suspension—the inset presents the higher magnification micrograph of the powder particles showing details of the particles in size and morphology (b) Particle size distribution of YAG particles in the as-received suspenion (c) Rietveld refinement of the XRD scan profile of the powder dried out from the as-received YAG suspension showing crystalline phase composition of YAG and Y_2O_3.

(a)) appear smaller compared to those on the S-YAG coating (Fig. 7(b)). The magnified view of the bumps on each of the two coatings is shown as insets; each presents a cluster of particles.

3.2.3. *Phase composition of coatings due to deposition process*

The Rietveld refinement analysis of the XRD scan of the SP-YAG and the S-YAG coating top surface was done to evaluate the presence of YAG or other phases from the Al-Y-O system ($AlYO_3$ (YAP) and $Y_4Al_4O_9$ (YAM)) in the as-sprayed topcoats. In case of inhomogeneous decomposition of the solution precursor, the coating could also present Al_2O_3 (aluminium oxide) and Y_2O_3 (yttrium oxide) [4]. The results of the analysis are shown in (Fig. 8(a) and (b)). The SP-YAG coating has ~10 wt % crystallinity, the coating is mainly amorphous as shown by the humps in the XRD scan profile (Fig. 8(a)) with their maximums centred at ~32.0° and ~47.5° 2θ respectively. The crystalline contents of the SP-YAG coating present 73.34% of YAG ($Y_3Al_5O_{12}$) and 26.66% of hexagonal YAP ($AlYO_3$). The S-YAG coating (Fig. 8(b)) on the other hand has ~12% crystallinity; with the centre of the amorphous humps at ~31.5° and ~48.9° 2θ respectively. Its crystalline content has 90.16% YAG ($Y_3Al_5O_{12}$) and 9.84% hexagonal YAP ($AlYO_3$).

3.3. *Thermal cycling*

The macroscopic images of the thermally cycled samples are shown in Fig. 9, where it can be appreciated that the SP-YAG coatings showed the first signs of failure after the fifth cycle, but a large part of the SP-YAG coting remained attached to the bond coat. However, 20% of failure was reached after the tenth cycle. In the S-YAG coatings, the first sign of failure appeared after 50 cycles as small spallation at the edge of the samples, and the debonding of the topcoat was complete between the cycles of 60th and 70th.

The top surface morphologies of the thermally cycled SP-YAG coating and the S-YAG coating after failure are shown in Fig. 10 (a) and (b), respectively. Each one presents micro-cracks, bright and dark patches in the BSE images showing the spallation sites. The micro-cracks appear to originate from the spallation sites.

The cross-section of the thermally cycled SP-YAG and S-YAG are shown in Fig. 11 (a) and (b), respectively. The cross-section of the sample with the SP-YAG topcoat (Fig. 11(a)) shows regions of topcoat spallation; the TGO layer presents a thickness of ~6 µm. The magnified view of a spallation region is shown as an inset and EDX spectra collection points (see Table 4). The EDX spectrum of the TGO layer region marked 2 shows Al (34.1%) and O (65.6%) as its main compositional elements with traces of Cr (0.2%) and Ni (0.1%). Spectrum 3 shows an additional element as Cr, Co, and Ni. The residual topcoat marked as 4 presents Al (19.7%) Y (13.7%) and O (65.8%) as its major elements while Cr, Co and Ni are detected in a lower proportion.

Fig. 11(b) shows the cross-section of a S-YAG sample after thermal cycling test. The magnified view of the failure region is shown as an inset with the corresponding EDX spectra collection points (see Table 4). It shows the TGO layer (~3 µm in thickness); its EDX spectra marked 6 shows only Al (34.1%) and O (65.9%) as its compositional elements. Spectra 7 collected on the remaining topcoat shows Al (19.3%) Y (13.9%) and O (66.5%) as its main constituents.

The XRD of the SP-YAG and S-YAG samples after their thermal cycling are shown in Fig. 12. The two coatings show the same phase compositions, and no amorphous phase is detected after the thermal cycling. YAG ($Y_3Al_5O_{12}$) from the topcoat is detected as the main phase. The Co from the bond coat is also detected along with corundum (α-alumina), formed as TGO from the oxidation of the bond coat.

4. Discussion

4.1. *YAG coating formation*

The YAG coatings obtained from solution precursor (SP-YAG) are

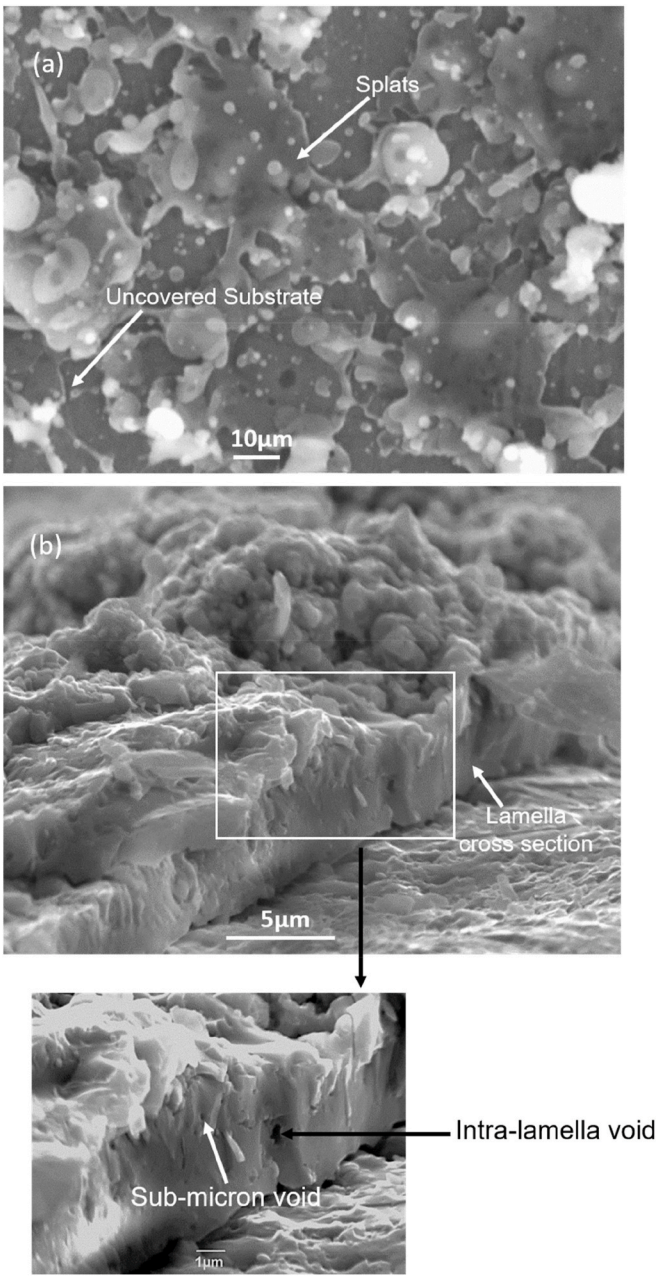

Fig. 4. SE scanning electron micrograpgh of (a) molten SP-YAG topcoat splats collected on mirror polished AISI 304 stainless steel showing the splat morphology and spread after impact (b) fractograpgh of SP-YAG topcoat showing lamella cross-section and intra-lamella void, with a high magnificaiton image in the inset.

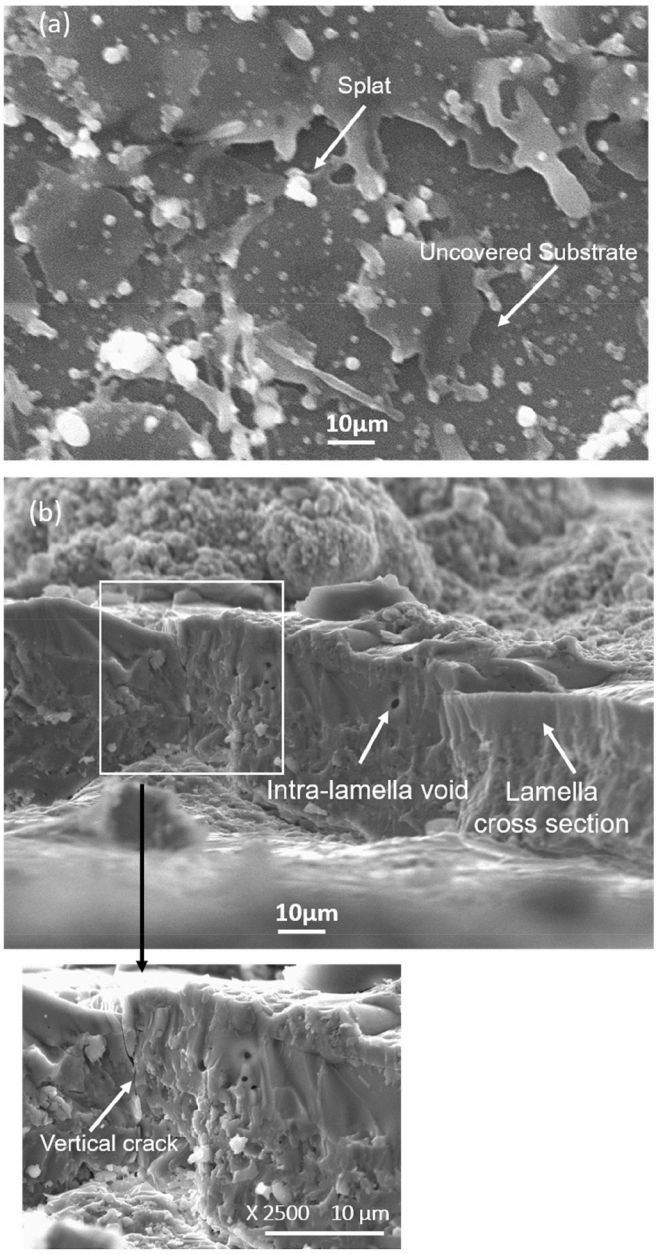

Fig. 5. SE scanning electron micrograpgh of (a) molten S-YAG topcoat splats collected on mirror polished AISI 304 stainless steel showing the splat morphology and spread after impact (b) fractograpgh of S-YAG topcoat showing lamella cross-section and intra-lamella void, with a higher magnificaiton image in the inset.

built from molten splats as well as the YAG coatings obtained from the YAG suspension (S-YAG); however, the splat formation mechanism of the two coatings set them apart. SP-YAG leads to the formation of thin coatings with a build-up around 1.65 µm/pass that produced a dense coating structure with no vertical cracks and the presence of evenly distributed porosity. The deposition of the S-YAG was faster, observing a deposition of 3.48 µm/pass with pores distributed randomly and vertical and horizontal cracks also detected in the coating.

The S-YAG formed from the evaporation of the carrier medium, melting and solidification of YAG particles upon impact on the substrates—a mechanism already reported for SHVOF thermal sprayed ceramics [28,29]. A coating microstructure is influenced by its building block: fully molten, semi-molten and unmolten splats depending on the coating formation mechanism [30].

The SP-YAG formation involves the evaporation of the solvent (water) and the thermal decomposition of the precursors (yttrium nitrate and aluminium nitrate) followed by the melting of the formed particles and final solidification upon impact [31]. The decomposition of the precursors implies an additional endothermic reaction process that forces proportionate cooling of combusted gases and the flame downstream at the gun exit, this explains why the temperature of the SP-YAG particles measured at spray distance (85 mm from the gun exit) was ~1623 °C as against the 2927 °C in the combustion chamber (from numerical models not shown here) [32]. Also, it explains the difference in measured in-flight temperature between SP-YAG and S-YAG. The S-YAG particles have retained much of its thermal energy to have a temperature of 1992 ± 60 °C as it was only cooled due to thermal energy

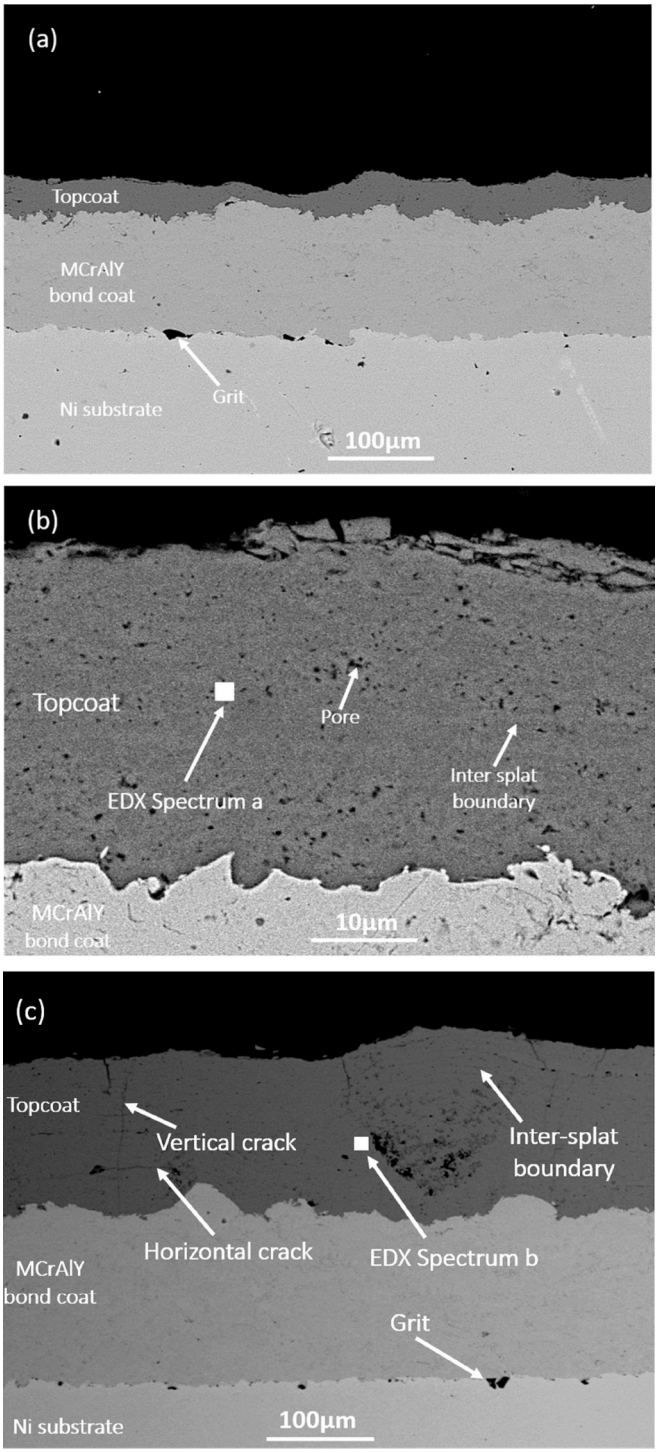

Fig. 6. Back scattered electron (BSE) scanning electron micrograph showing the cross section of as-sprayed topcoats on bond coated nickel (Ni) alloy substrate with a white square dot designating the EDX spectrum collection spots (a and b, see Table 3) (a) SP-YAG topcoat (b) higher magnification of the SP-YAG topcoat showing pores, inter splat boundary and the interface with the MCrAlY bond coat, (c) S-YAG topcoat with pores, vertical and horizontal cracks, inter splat boundary and the interface of the S-YAG topcoat with the MCrAlY bond coat.

lost from water evaporation. In contrast, the SP-YAG particle temperature (1623 ± 49 °C) resulted from thermal energy lost due to cooling as a result of evaporation and endothermic heat of reaction consumed from the combusted gases. More so, the variation in the measured temperatures could not have been due to the resident time of the feedstock in the

Table 3
EDX analysis of the atomic % of Al, O and Y in the as-sprayed SP-YAG and S-YAG topcoats.

Elements	Topcoat samples	
	SP-YAG (spectrum a)	S-YAG (spectrum b)
O	60.6	61.3
Al	23.3	22.7
Y	16.2	16.0
Total	100.0	100.0

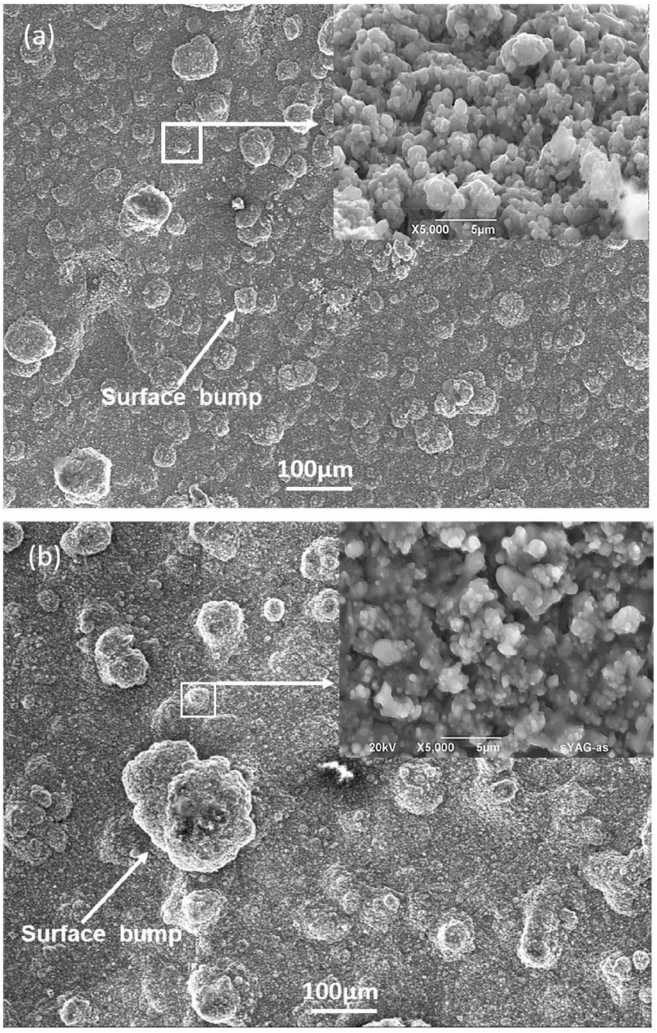

Fig. 7. SE scanning electron micrograph showing surface morphology of (a) SP-YAG topcoat with randomly distributed bumps and (b) S-YAG topcoat with randomly distributed bumps.

flame—both the SP-YAG and the S-YAG have the same inflight velocity of ~ 855 m/s.

Furthermore, the SP-YAG precursor solution was injected into a mixture of hot turbulent combusted gases and flame with central static temperature in excess of 2927 °C [32]. The combination of the DTG results, the FTIR and the XRD diffractogram of the calcined samples provide insight into how the phases in the SP-YAG form. The formation process presents two endothermic amorphous stages: the first (150–450 °C) due to decomposition of the nitrates, and the second (500–900 °C) due to aluminium ion (Al^{3+}) coordination site rearrangement and yttrium ion (Y^{3+}) substitution [33,34]. The decomposition of the nitrate groups is complete at around 450 °C, as shown by the

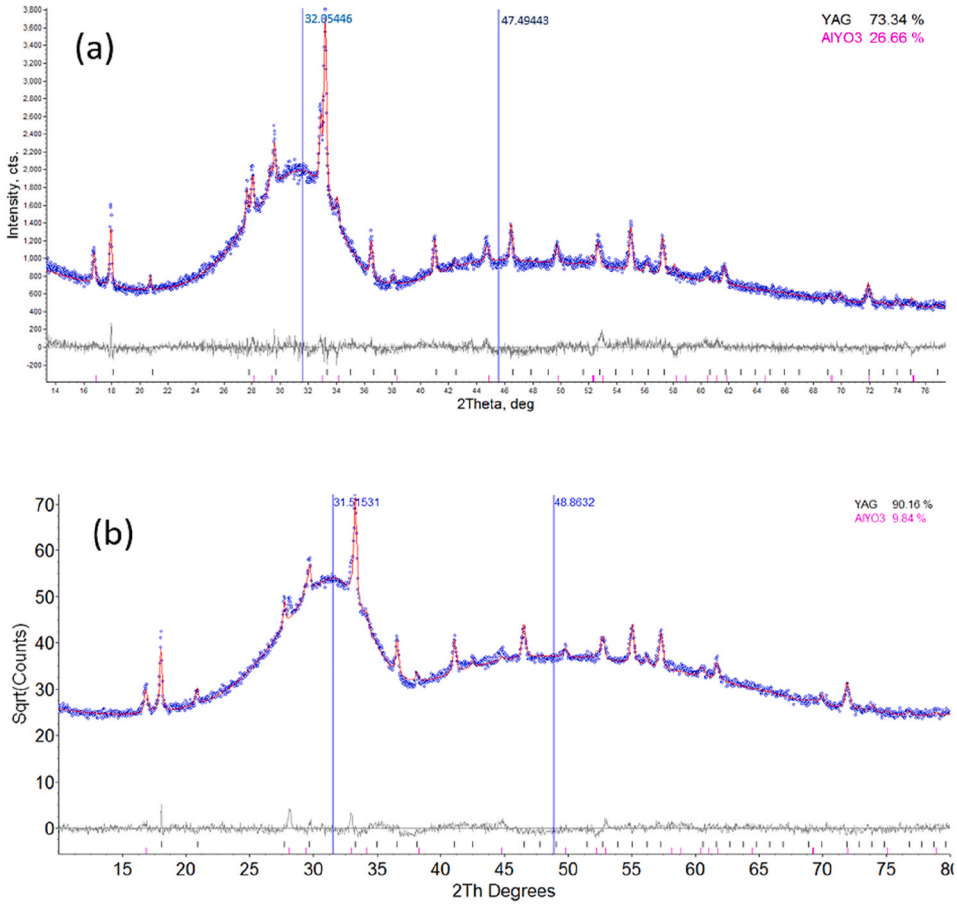

Fig. 8. Rietveld refinement profile of the XRD scan of the as-sprayed (a) SP-YAG topcoat (b) S-YAG topcoat; each showing amorphous humps and two crystalline phase compositions with varying proportions.

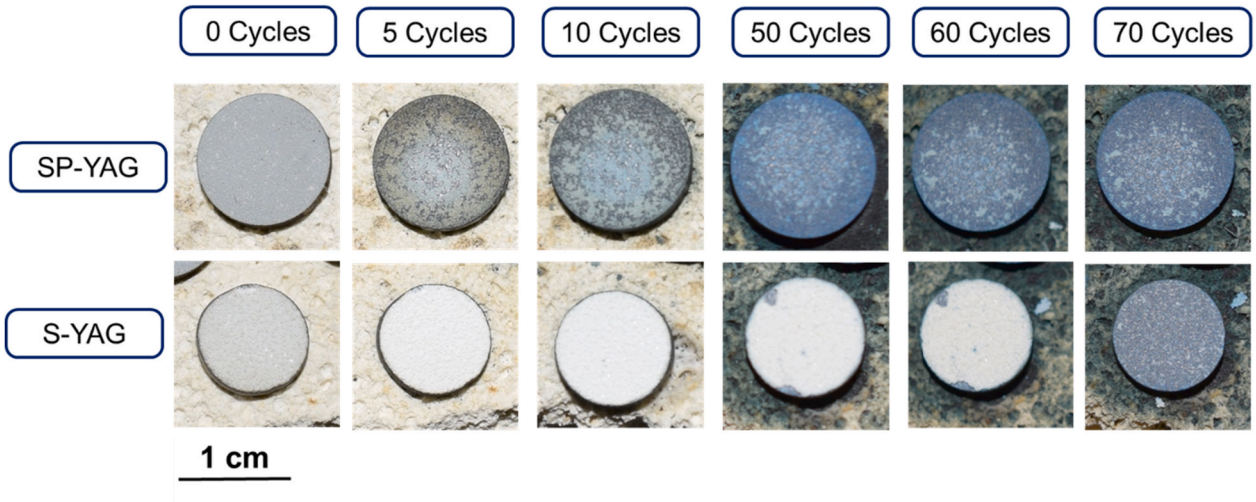

Fig. 9. Digital camera images of selected thermal cycled samples after different cycles.

DTG results. The FTIR analysis of the samples calcined at 450 and 750 °C showed a marginal contribution of the nitrate bands as some nitrates remain as impurity in the calcined samples, and the samples remained amorphous as it was revealed by the XRD analysis. The amorphous phase at this stage (750 °C) represents the onset of the YAG phase formation since YAG forms by aluminium ion (Al^{3+}) coordination site rearrangement and yttrium ion (Y^{3+}) substitution. The SP-YAG coating formation is characterized by the atomization of the solution precursor developing high surface area when it was injected into the combustion chamber that also provides the high reaction temperature (2927 °C). These two conditions facilitate the rapid evaporation of the liquid medium and the decomposition of the precursor reactants, leading to the rapid melt and quench of the YAG precursor.

The two coatings are mostly amorphous, SP-YAG shows lower crystallinity of 10% compared to the 12% of the S-YAG; however, this disparity is not significant. The crystalline compositions of the two

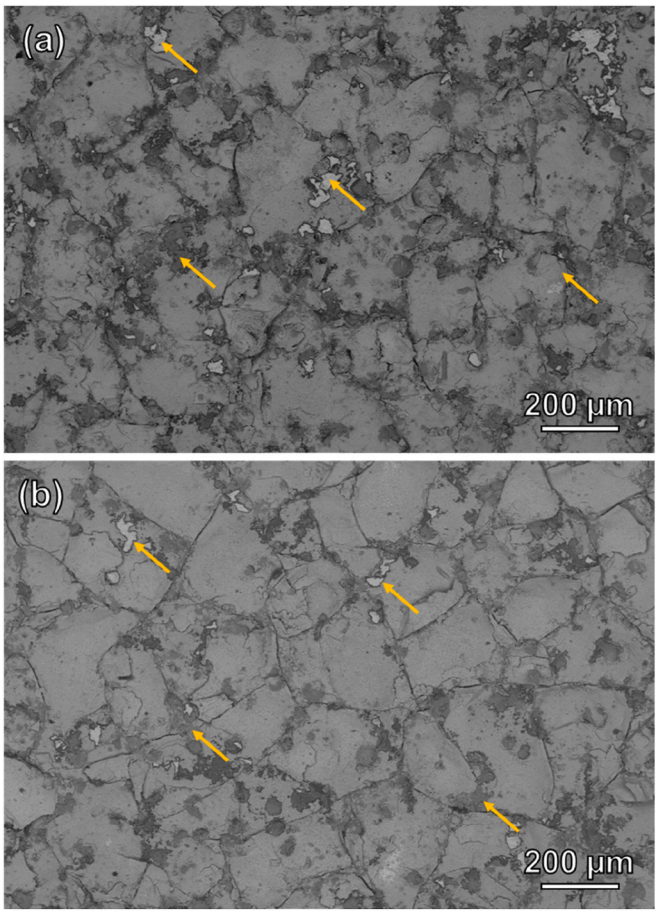

Fig. 10. BSE scanning electron micrograph showing spallation sites (arrows) on the surface of the (a) thermally cycled SP-YAG topcoat (b) thermally cycled S-YAG topcoat, respectively.

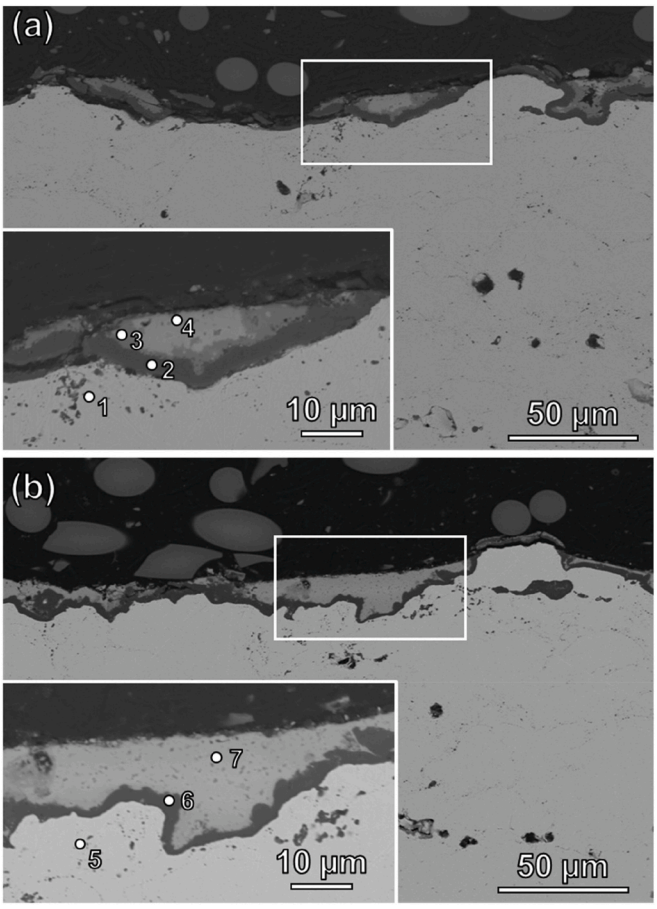

Fig. 11. BSE scanning electron micrograph showing the cross section of (a) thermally cycled SP-YAG topcoat (b) thermally cycled S-YAG topcoat respectively with the TGO layer and white dots designating EDX spectrum collection spots (see Table 4).

coatings presents no variation; each one shows cubic YAG and hexagonal YAP. In a reaction with intermediate products, the least stable reaction product precipitates first based on the Ostwald rule of successive formation [35]. The hexagonal structure of YAP forms first from the amorphous Al_2O_3-Y_2O_3 system. This explains why both the SP-YAG and the S-YAG contain YAP (hexagonal), although in varying quantities as the two coatings suffered a different quenching process. The presence of YAG and YAP in coatings sprayed from YAG powder was reported by Weyant and Faber [7]—the occurrence was attributed to the rapid quenching effect of thermal spray processes. Weyant and Faber [7] also indicated that the crystallinity is highly influenced by the flame power and spray distance, increasing with higher flame power and shorter spray distances. The presence of a similar amount of amorphous phase and a small amount of crystalline phase in both samples indicates that both methods produced the complete melting of the particles and subsequent partial crystallization of YAG and YAP.

The composition of the amorphous phase in the two coatings shows no significant difference in the atomic % compositions of Al and Y as revealed by EDX analysis (see Table 3), the EDX results of the two coatings suggest the amorphous contents should be an amorphous phase with YAG composition.

4.2. Phase evolution and failure modes

At the test temperature 1100 °C, amorphous YAG [7] and hexagonal YAP [23] present in the SP-YAG and S-YAG samples transform to crystalline YAG. The amorphous-crystalline transition proceeds with volume reduction due to the establishment of structural order. The kinetics of amorphous to crystalline YAG transition suggests the transformation completes in less than 20 min between 900 °C and 1100 °C [7]—this suggests the two coatings have transformed fully to YAG in the first cycle of the thermal cycle test, and the complete transformation is detected after the thermal cycling (see Fig. 12). The temperature range prevents the possibility of forming intermediate phases of hexagonal and cubic YAP in succession before the formation of YAG from the thermal decomposition cubic YAP to yield YAG and YAM [34].

The two coatings studied in this work show indication of failure due to a mixture of different phenomena. Factors such as reduced strain compliance due to a lack of porosity and the amorphous to crystalline transition could also play a significant role in the failure observed for

Table 4
EDX analysis of the cross-section of the thermally cycled SP-YAG and S-YAG showing atomic % of elemental composition.

Elements	SP-YAG spectra				S-YAG spectra		
	1	2	3	4	5	6	7
O	–	65.6	66.9	65.7	–	65.9	66.5
Al	9.7	34.1	21.2	19.7	9.5	34.1	19.3
Y	–	–	–	13.7	–	–	13.9
Ti	0.4	–	–	–	0.5	–	–
Cr	22.1	0.2	2.6	0.6	22.2	–	0.3
Co	32.6	–	5.2	0.1	32.6	–	–
Ni	34.8	0.1	4.2	0.2	35.2	–	–
S	0.4	–	–	–	–	–	–
Total	100	100	100	100	100	100	100

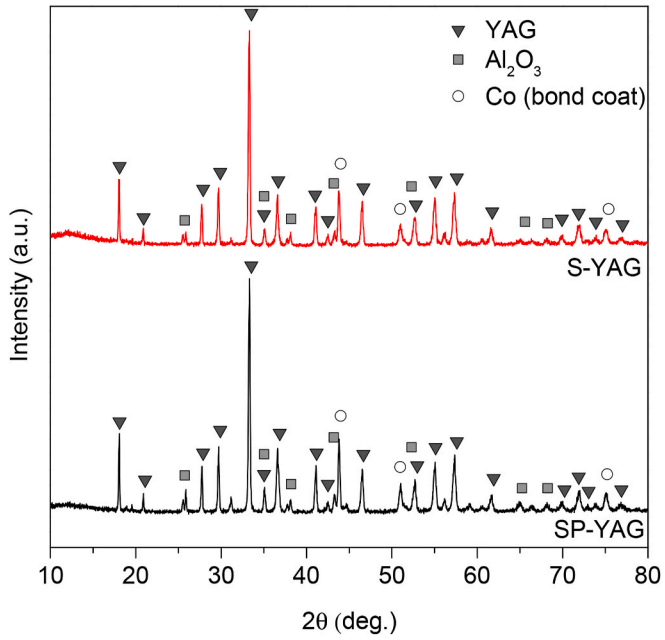

Fig. 12. X-ray diffraction patterns of SP-YAG and S-YAG after thermal cycling failure.

both coatings. It would be worth pointing out that nearly complete crystalline YAG coatings produced with APS showed longer lifetimes [7]. The mismatch between topcoat and bond coat thermal expansion, and the failure of TGO could also contributed to the failure of the coatings here.

The early failure of the SP-YAG sample could be attributed to the absence of vertical cracks and limited porosity that reduces its strain compliance. The S-YAG, on the other hand, has vertical cracks that could have ensured improved strain tolerance of the coating. The spallation of the two coatings could also have a contribution from amorphous to crystalline transition, this contribution should be minimal because the transition completes in the first cycle.

5. Conclusions

This paper presents for the first time, SP-HVOF and SHVOF thermal spray of YAG topcoats. The as-sprayed and thermally cycled topcoats present distinct microstructural evolution, which affects the topcoat performance. The following conclusions can be drawn:

- The SP-YAG formed a dense coating that contains micro pores as main defects, while the S-YAG has vertical and horizontal micro cracks, pores and inter splat boundaries.
- The as-sprayed SP-YAG and S-YAG were mainly composed of amorphous phase presenting a small proportion of YAP and YAG phases.
- The premature failure of the SP-YAG coating was mainly related to its dense nature and its inability to accommodate thermal stresses in the microstructure, while the S-YAG had a higher thermal cycling lifetime as the microstructure can accommodate the thermal stresses caused by the thermal cycling.

Declaration of competing interest

The authors declare that they have no known competing financial interests or personal relationships that could have appeared to influence the work reported in this paper.

Acknowledgment

This work was supported by the Engineering and Physical Sciences Research Council [EP/M01536X/1]. The authors acknowledge experimental support offered by Mr. N. Sharif of the School of Chemistry in the development of the solution precursor, Mr. R. Screaton and Mr. J. Kirk helped with the spraying of the coatings. The authors appreciate the support of Baikowski for providing the YAG suspension used in this work. The authors thank the Nanoscale and Microscale Research Centre (nmRC) for providing access to characterization instruments. Petroleum Technology Development Fund (PTDF/ED/PHD/OTA/872) supports Tunji Owoseni under the overseas scholarship scheme.

References

[1] N.P. Padture, M. Gell, E.H. Jordan, Materials science - thermal barrier coatings for gas-turbine engine applications, Science 296 (5566) (2002) 280–284.
[2] D.R. Clarke, M. Oechsner, N.P. Padture, Thermal-barrier coatings for more efficient gas-turbine engines, MRS Bull. 37 (10) (2012) 891–898.
[3] A.J. Allen, et al., Microstructural characterization studies to relate the properties of thermal-spray coatings to feedstock and spray conditions, Surf. Coating. Technol. 146 (2001) 544–552.
[4] M. Gell, et al., Higher temperature thermal barrier coatings with the combined use of yttrium aluminum garnet and the solution precursor plasma spray process, J. Therm. Spray Technol. 27 (4) (2018) 543–555.
[5] H.B. Guo, R. Vassen, D. Stover, Atmospheric plasma sprayed thick thermal barrier coatings with high segmentation crack density, Surf. Coating. Technol. 186 (3) (2004) 353–363.
[6] C.A. Johnson, et al., Relationships between residual stress, microstructure and mechanical properties of electron beam–physical vapor deposition thermal barrier coatings, Surf. Coating. Technol. (1998) 108–109, 80-85.
[7] C.M. Weyant, K.T. Faber, Processing-microstructure relationships for plasma-sprayed yttrium aluminum garnet, Surf. Coating. Technol. 202 (24) (2008) 6081–6089.
[8] Z. Zou, et al., Role of internal oxidation on the failure of air plasma sprayed thermal barrier coatings with a double-layered bond coat, Surf. Coating. Technol. 319 (2017) 370–377.
[9] C. Viazzi, et al., Structural study of metastable tetragonal YSZ powders produced via a sol–gel route, J. Alloys Compd. 452 (2) (2008) 377–383.
[10] L. Li, N. Hitchman, J. Knapp, Failure of thermal barrier coatings subjected to CMAS attack, J. Therm. Spray Technol. 19 (1) (2010) 148–155.
[11] M. Bai, et al., Microstructure and phase stability of suspension high velocity oxy-fuel sprayed yttria stabilised zirconia coatings from aqueous and ethanol based suspensions, J. Eur. Ceram. Soc. 38 (4) (2018) 1878–1887.
[12] R. Vassen, A. Stuke, D. Stover, Recent developments in the field of thermal barrier coatings, J. Therm. Spray Technol. 18 (2) (2009) 181–186.
[13] N.P. Padture, P.G. Klemens, Low thermal conductivity in garnets, J. Am. Ceram. Soc. 80 (4) (1997) 1018–1020.
[14] Y.J. Su, et al., Thermal conductivity, phase stability, and oxidation resistance of Y3Al5O12 (YAG)/Y2O3–ZrO2 (YSZ) thermal-barrier coatings, Oxid. Metals 61 (3) (2004) 253–271.
[15] J.S. Abell, et al., An investigation of phase stability in the Y2O3-Al2O3 system, J. Mater. Sci. 9 (4) (1974) 527–537.
[16] M. Gell, et al., Higher temperature thermal barrier coatings with the combined use of yttrium aluminum garnet and the solution precursor plasma spray process, J. Therm. Spray Technol. 27 (4) (2018) 543–555.
[17] R. Kumar, et al., Low thermal conductivity yttrium aluminum garnet thermal barrier coatings made by the solution precursor plasma spray: Part II-planar pore formation and CMAS resistance, J. Therm. Spray Technol. 27 (5) (2018) 794–808.
[18] Y.Q. Wu, J. Du, K.L. Choy, Novel deposition of columnar Y3Al5O12 coatings by electrostatic spray-assisted vapor deposition, J. Am. Ceram. Soc. 89 (1) (2006) 385–387.
[19] R. Kumar, et al., CMAS behavior of yttrium aluminum garnet (YAG) and yttria-stabilized zirconia (YSZ) thermal barrier coatings, Surf. Coating. Technol. 327 (2017) 126–138.
[20] R. Kumar, et al., Low thermal conductivity yttrium aluminum garnet thermal barrier coatings made by the solution precursor plasma spray: Part I-processing and properties, J. Therm. Spray Technol. 27 (5) (2018) 781–793.
[21] L. Gu, et al., Phase stability of plasma sprayed YAG–YSZ composite beads/coatings at high temperature, J. Eur. Ceram. Soc. 33 (15) (2013) 3325–3333.
[22] G. Bolelli, et al., Microstructural and tribological investigation of high-velocity suspension flame sprayed (HVSFS) Al2O3 coatings, J. Therm. Spray Technol. 18 (1) (2008) 35.
[23] P. Ramanujam, et al., A comparative study of the synthesis of nanocrystalline Yttrium Aluminium Garnet using sol-gel and co-precipitation methods, Ceram. Int. 40 (3) (2014) 4179–4186.
[24] S. Saeidi, Thesis (PhD), in: Microstructure, Oxidation & Mechanical Properties of As-Sprayed and Annealed HVOF & VPS CoNiCrAlY Coatings [electronic resource]/ Saman Saeidi, M. University of Nottingham. Theses. Mechanical and E. Manufacturing, University of Nottingham, 2011.

[25] G. Mauer, R. Vassen, D. Stover, Comparison and applications of DPV-2000 and accuraspray-g3 diagnostic systems, J. Therm. Spray Technol. 16 (3) (2007) 414–424.
[26] P. Scardi, M. Leoni, Whole powder pattern modelling, Acta Crystallogr. A 58 (2) (2002) 190–200.
[27] Y. Sang, et al., Yttrium aluminum garnet nanoparticles synthesized by nitrate decomposition and their low temperature densification behavior, J. Alloys Compd. 490 (1) (2010) 459–462.
[28] T.A. Owoseni, et al., Suspension high velocity oxy-fuel (SHVOF) spray of delta-theta alumina suspension: phase transformation and tribology, Surf. Coating. Technol. 371 (2019) 97–106.
[29] M. Bai, et al., Suspension high velocity oxy-fuel spraying of a rutile TiO 2 feedstock: microstructure, phase evolution and photocatalytic behaviour, Ceram. Int. 43 (17) (2017) 15288–15295.
[30] L. Pawlowski, Finely grained nanometric and submicrometric coatings by thermal spraying: a review, Surf. Coating. Technol. 202 (18) (2008) 4318–4328.
[31] D. Chen, E.H. Jordan, M. Gell, Effect of solution concentration on splat formation and coating microstructure using the solution precursor plasma spray process, Surf. Coating. Technol. 202 (10) (2008) 2132–2138.
[32] S. Chadha, et al., A computational and experimental investigation into radial injection for suspension high velocity oxy-fuel (SHVOF) thermal spray, J. Therm. Spray Technol. 28 (6) (2019) 1126–1145.
[33] J. Carda, et al., A Rietveld study of the cation substitution between uvarovite and yttrium-aluminum synthetic garnets, obtained by sol-gel method, Cryst. Res. Technol. 29 (3) (1994) 387–391.
[34] O. Yamaguchi, K. Matui, K. Shimizu, formation of YAIO3 with garnet structure, Ceram. Int. 11 (3) (1985) 107–108.
[35] R.A. Van Santen, The Ostwald step rule, J. Phys. Chem. 88 (24) (1984) 5768–5769.